

A novel non-invasive intervention for removing occlusions from shunts using an abrading magnetic microswarm

A. Moghanizadeh⁺, H. Khaksar⁺, and A. K. Hoshidar^{*}, *Member, IEEE*

Abstract-

Objective: Shunts are often employed as internal medical devices for draining aberrant fluids from organs. However, depositions of calcification in the shunt walls lead to its failure, requiring frequent replacements. The current surgical procedures for implanting shunts are invasive. **Methods:** This paper introduces a novel, non-invasive approach for eliminating shunt deposits. In this non-invasive intervention, a swarm of magnetic nanoparticles (MNPs) guided by an external magnetic field removes the shunt deposition. A prototype device was fabricated to provide a proof of concept. MNPs were steered within the shunt channel containing calcification layers and successfully abraded the deposition layer. The proof-of-concept experiments used a moving magnetic field ranging from 0.1 to 0.3 T and a velocity between 1 to 12 cm/s. The average nanoparticle size was 45nm. Five diverse contact theories predicted the amount of wear and indentation depth created by the abrading microswarm. **Results:** Experimental results confirm that MNPs under a moving magnetic field can abrade shunt deposits. Also, there is a direct relation between the intensity of the magnetic field, the speed of magnet movement, and the rate of abrading the calcification deposits. The simulation results showed that the Hoepflich model deviated 12.1% from the experimental results and was the most suitable model. **Conclusion & significance:** This research has introduced a novel minimally invasive approach to remove shunt depositions that can reduce the number of revision surgeries and prevent surgical complications.

Index Terms- Shunt deposit- Calcification- Swarm of magnetic nanoparticles - Steering, Non-invasive method.

I. INTRODUCTION

A shunt usually consists of a peritoneal tube placed in a cavity to receive excess fluid [1]. Over the last 50 years, shunts have often been employed as internal medical devices to treat a variety of medical conditions by draining aberrant fluids from various organs, such as in hydrocephalus [2]. Hydrocephalus is a medical condition in which an abnormal amount of cerebrospinal fluid (CSF) accumulates in the ventricles (or cavities) of the brain. A shunt is placed vertically from the patient's brain to another area of the patient's body to drain the excess CSF [3].

Shunt malfunction is a serious challenge, especially in cases where repeated surgeries are necessary throughout the patient's life. There is a high risk of recurrent surgery for elderly patients

sixty-five years of age and older [3] and children [4]. In addition, as the recurrent surgeries or the non-invasive approach presented here need monitoring (MRI/CT/X-ray), the healthcare costs will be increased [5]. Fifty percent of shunts fail in two years [6], [7], and 85% percent of shunt patients will undergo two shunt revision surgeries at least ten years after the initial surgery [8]. Occlusions are the most frequent cause of failure of conventional shunts [6]. Previous studies have confirmed that after roughly 24 months, over 50% of shunts need replacement reconsideration [7].

Research has demonstrated that when the blood encephalic barrier is efficient, normal cerebrospinal fluid is composed of water and small ions (i.e., smaller ion salts) [8]. However, a large distribution of small particle sizes can progressively lead to an occlusion [9]. One of the primary causes of shunt malfunction is the formation of a layer of calcification or sediment inside the shunt [10]. The creation of this layer not only narrows and obstructs the passage of liquid but also affects the mechanical properties of the shunt by reducing its flexibility, causing damage to the shunt [11].

Researchers have suggested a variety of methods to eliminate calcification, but these methods have known side effects or disadvantages. Surgery to replace the occluded shunt has been proposed [12]. However, surgery not only has a high risk, especially for the elderly and children but also can cause side effects such as infection.

Using a rotating tool to abrade the inside of the shunt is a minimally invasive technique for removing the calcification from the shunt. The tool is inserted into the shunt from the right atrium with a catheter. However, the removal is usually not straightforward due to the frequent presence of adhesions to the endocardial structures. Furthermore, a sizeable atrial thrombus makes the removal procedure riskier. There is also the possibility of damaging the shunt with the rotating tool [13]. Researchers have investigated using low-frequency (20 kHz) extensional waves to unblock shunts by creating cavitation. In this process, the cavitation disintegrates the calcification layers. However, inserting a tip wire in the shunt is required in this approach, which is considered invasive [14]

A thoracotomy is another technique for cleaning a shunt, especially when a blood clot blocks the shunt. However, the

This work is supported by the University of Essex, Faculty of Health and Science, Department of Computer Science and Electronic Engineering, Robotics and Embedded System (RES) research group.

A. Moghanizadeh⁺ and H. Khaksar⁺ equally contributed to this work.

A. Moghanizadeh is with the Department of Materials Engineering, Isfahan University of Technology, Isfahan, 84156-83111, Iran.

H. Khaksar and A. K. Hoshidar are with the School of Computer Science and Electronic Engineering, University of Essex, Colchester, CO4 3SQ, UK
A.Kafashhoshidar@Essex.ac.uk

thoracotomy might cause infection at the catheter entry site [15]. Using short pulses of infrared light generated by a Holmium: YAG (Ho: YAG) surgical laser to photofragment the clot has also been investigated as a method to remove the occlusions and restore flow in ventricular shunts. Although a laser is a minimally invasive approach, this technique requires inserting a light fibre into the shunt, which requires an invasive procedure [16].

Consequently, a novel, non-invasive alternative to wirelessly clean a shunt is vital. Manipulating a microswarm (collective movement of magnetic nanoparticles) can be used for this purpose. Some studies used the motion of nanoparticles to eliminate blood clots [17]. Methods such as a rotating magnetic field [18] and the Helmholtz coil system [19],[20] have been used to move and control the swarm. However, they did not investigate this method for shunt abrading.

Therefore, this study investigates a new method to remove calcification wirelessly inside the shunt using magnetic abrasive microswarms.

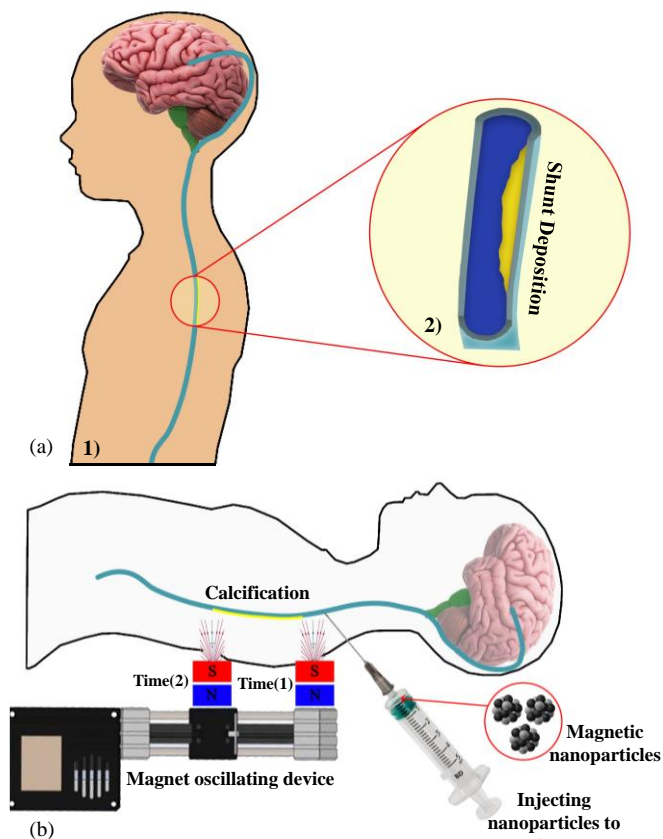


Fig.1. Schematic of shunt deposition removal. (a) Shunt position in body (1. A shunt is a hollow tube installed in the brain to drain cerebrospinal fluid and discharge it to an alternative place in the body. 2. Calcification in the shunt causes an obstruction or reduction of the inner diameter of the shunt). (b) Mechanism of calcification removal using magnetic nanoparticles under an oscillating magnetic field. (The permanent magnet oscillates between positions 1 and 2 to remove the calcification.)

The overall process appears in Fig.1. After injecting magnetic nanoparticles into the shunt, the magnetic field, generated by a powerful permanent magnet located on the body surface, oscillates the magnetic nanoparticles along the shunt

channel. The magnetic field captures the abrasive magnetic nanoparticles, which accumulate at the site of the magnetic field. Oscillation of the magnetic field will remove the calcification by slightly abrading its surface.

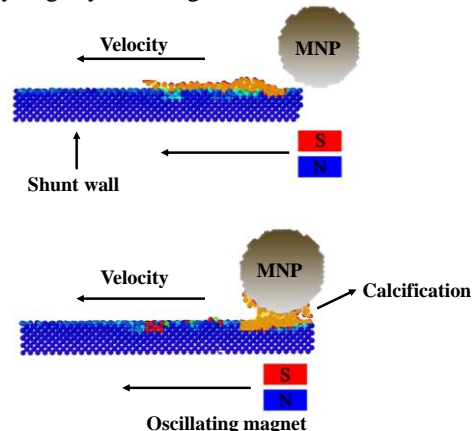


Fig.2. Mechanism of calcification surface removal using magnetic nanoparticles under a magnetic field.

The process of removing the calcification layer inside a shunt appears in Fig. 2. The proposed technique wirelessly removes the calcification with a minimally invasive intervention using a swarm of magnetic particles. Since the shunts eventually discharge into the stomach or another region in the body pathway, the nanoparticles at the end of the process can be transferred to the stomach using either a guiding magnetic field or body fluid. Magnetic nanoparticles have very high biocompatibility and, therefore, will not cause toxicity.

To minimize the risk of unintentional damage to the vessel, the experiments developed suitable contact models and simulated the indentation depth. Experiments were carried out in vitro to investigate effective parameters for cleaning the shunt, including magnetic field strength and nanoparticle velocity. This paper first introduced the electromagnetic models and the mechanics of contact. Next, it described the proof-of-concept experiment for the abrading process. Finally, it compared the results of indentation depth in the predictive model and the experimental results.

II. MODELLING ABRADING BY MAGNETIC MICROSWARM

A. Modelling assumptions

The following hypotheses simplify the computational operations:

- Magnetic field assumptions:
 - The magnetic field is constant during the process.
 - The magnetic properties of nanoparticles are constant during operation.
 - The debris produced from the ablation during the process has an insignificant effect on the process.
 - The effect of fluid flow on the movement of nanoparticles has not been considered (due to the high magnetic field effect).
- Micro/nano magnetic abrasive particle assumptions:
 - Abrasive particles have the same size; nominal average values are used.

- The particle shape is considered to be polyhedral to encompass all geometric shapes. However, the experiments used nanoparticles with approximately spherical shapes.
 - The applied force on each abrasive particle is constant.
 - The magnetic abrasive particles are not degraded during the process.
 - The mechanical properties of the deposited material (calcification) do not change during the operation.
- Artery deposit material (calcification assumptions):
- Chemical processes do not play a role in solubilizing the calcification.
- Significant forces apply in the mathematical model:
- The effects of gravitational forces, buoyancy forces, and inertial forces are relatively small for nanoparticles and are considered negligible.

B. Electromagnetic model

This section presents the general equations related to the electromagnetic force. Considering $\mathbf{B}(3 \times 1)$ is the magnetic field vector, the magnetic field is calculated in a three-dimensional space as:

$$\nabla \cdot \mathbf{B} = 0 \quad (1)$$

$$\nabla \times \mathbf{B} = 0 \quad (2)$$

Due to the presence of this magnetic field, a magnetic force and torque can be generated. Eq.3 shows the magnetic force, and Eq.4 shows the magnetic torque.

$$\mathbf{F} = (\mathbf{m} \cdot \nabla) \mathbf{B} \quad (3)$$

$$\boldsymbol{\tau} = \mathbf{m} \times \mathbf{B} \quad (4)$$

where $\mathbf{F}(3 \times 1)$ and $\boldsymbol{\tau}(3 \times 1)$ are vectors of force and magnetic torque, and $\mathbf{m}(3 \times 1)$ is the moment of the magnetic object. Based on Eq.1 to Eq.4, the magnetic force and torque are presented (Eq.5 and Eq.6):

$$\mathbf{F} = \begin{bmatrix} f_x \\ f_y \\ f_z \end{bmatrix} = \begin{bmatrix} m_x & m_y & m_z & 0 & 0 \\ 0 & m_x & 0 & m_y & m_z \\ -m_z & 0 & m_x & -m_z & m_y \end{bmatrix} \begin{bmatrix} \frac{\partial B_x}{\partial x} \\ \frac{\partial B_x}{\partial y} \\ \frac{\partial B_x}{\partial z} \\ \frac{\partial B_y}{\partial x} \\ \frac{\partial B_y}{\partial y} \\ \frac{\partial B_y}{\partial z} \end{bmatrix} \quad (5)$$

$$\boldsymbol{\tau} = \begin{bmatrix} \tau_x \\ \tau_y \\ \tau_z \end{bmatrix} = \begin{bmatrix} 0 & -m & m_y \\ m_z & 0 & -m_x \\ -m_y & m_x & 0 \end{bmatrix} \begin{bmatrix} B_x \\ B_y \\ B_z \end{bmatrix} \quad (6)$$

C. Calculation of contact mechanics

The main limiting factor in the presented minimally invasive intervention method is the lack of predictive modelling. The

abrading process has two phases: 1) initial contact (before moving) and 2) the microswarm movement. In this paper, for the first phase, we determine the amount of deformation in the calcification due to the applied magnetic force using contact models. For this purpose, we use line contact theories to determine the indentation depth and deformation in the contact process. The contact schematic of the problem appears in Fig.3.

Many contact theories cannot describe the line contact model because, in this contact type, one of the surfaces has an infinite radius. This section uses five different contact models for better evaluation. These models were developed for the elastic contact mode.

Eq.7 shows the amount of force versus indentation depth based on the Hertz contact model [21].

$$\delta_{\text{Hertz}} = F_{\text{Hertz}} L \pi E^* \left(2 \ln \left(\frac{4R_c}{a} \right) - 1 \right)^{-1} \quad (7)$$

Where, F_{Hertz} is the force based on the Hertz model, δ_{Hertz} is the indentation depth for the Hertz model, a is the contact radius, and E^* is the effective modulus of elasticity, which is calculated from Eq.8. E and ν are the modulus of elasticity and the Poisson's ratio.

$$E^* = \left(\frac{1-\nu_1^2}{E_1} + \frac{1-\nu_2^2}{E_2} \right)^{-1} \quad (8)$$

The relation between indentation depth and force for four contact models, Lundberg [22], Dowson [23], Nikpur [24], and Hoeprieh [25], is shown in Eq.9 to Eq.12, respectively.

$$\delta_{\text{Lundberg}} = 4 \left(\frac{F_{\text{Lundberg}}}{L \pi E^*} \right) \ln \left(\frac{L^2 \pi E^*}{F_{\text{Lundberg}}} \right) \quad (9)$$

$$\delta_{\text{Dowson}} = 4 \left(\frac{F_{\text{Dowson}}}{L \pi E^*} \right) \ln \left(\frac{L \pi E^* R_c \times e^{\frac{-\nu}{2(1-\nu)}}}{2 F_{\text{Dowson}}} \right) \quad (10)$$

$$\delta_{\text{Nikpur}} = 4 \left(\frac{F_{\text{Nikpur}}}{L \pi E^*} \right) \ln \left(\frac{L^2 \pi E^*}{F_{\text{Nikpur}}} \left(\frac{\sqrt{1 + \left(\frac{2H}{L} \right)^2} - 1}{\sqrt{1 + \left(\frac{2H}{L} \right)^2} + 1} \right)^{\frac{1}{2}} \right) \quad (11)$$

$$\delta_{\text{Hoeprieh}} = 4 \left(\frac{F_{\text{Hoeprieh}}}{L \pi E^*} \right) \ln \left(\frac{L \pi E^* H e^{\frac{-1}{2(1-\nu)} \sqrt{1 + \left(\frac{2H}{L} \right)^2}}}{F_{\text{Hoeprieh}}} \right) \quad (12)$$

where, F is the force in each model, L is the length of nanoparticles, R_c is the distance from the centre, and H is the shunt deposit. The characteristics of each model are in Table I. (Other information appears in Fig. 3. δ_m indicates the indentation depth created by the magnetic force).

D. Motion mode modelling in the abrading process

Fig.3 shows the important forces applied to the set of nanoparticles. It is assumed that the magnetic force F_m exerts at an angle β to the centre of the object.

The mode in which particles move on the substrate influences the contact force between magnetic nanoparticles and calcification. Based on the dimensions of the shunt and the sediment and nanoparticle assembly, two sliding and rolling motion modes can occur for the assembly. The force that opposes the motion of the nanoparticles is illustrated as friction force. Therefore, Eq.13 shows the sliding condition, and Eq.14 shows the rolling condition.

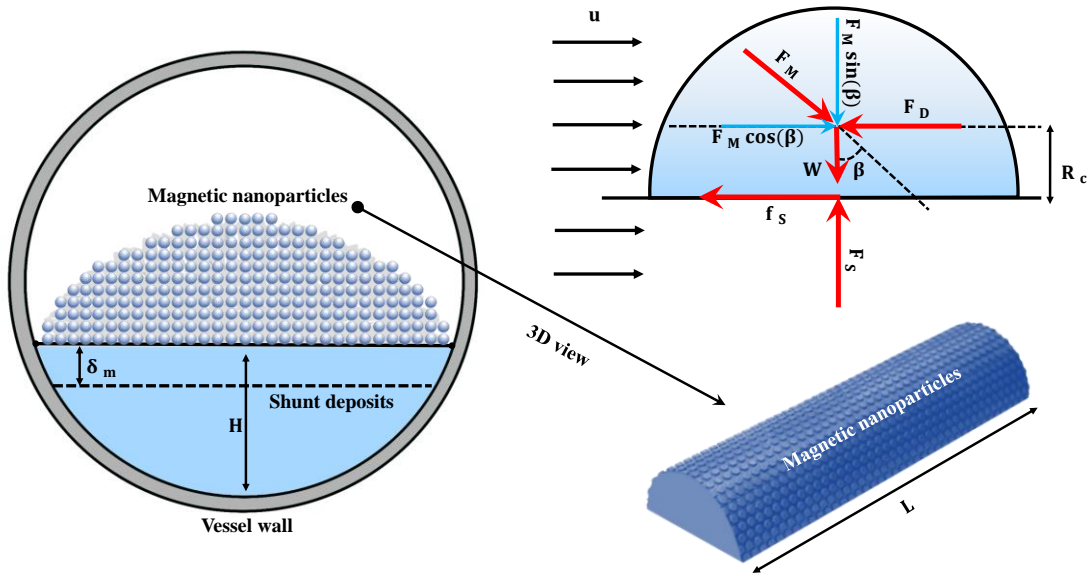


Fig.3. Contact mechanic schematic and geometrical information (forces applied to nanoparticles in the presence of friction force).

$$f_s > \mu_s F_s + \tau_s A_s \quad (13)$$

$$R_c f_s > \mu_{rs} F_s + \tau_{rs} A_s \quad (14)$$

where, f_s is the friction force, F_m is the magnetic force, R_c is the distance from the centre, A_s is the contact area, μ and τ are the friction coefficient and shear stress (τ_s , μ_s illustrates the sliding mode and τ_{rs} , μ_{rs} represents the rolling mode), and F_s is the normal force. According to Fig.3:

$$f_s = F_m \cos \beta - F_D \quad (15)$$

$$F_s = F_m \sin \beta + W \quad (16)$$

where, F_D is the drag force, and W is the weight. Eq. 17 and Eq.18 calculate the final values of sliding and rolling modes.

TABLE I
DESCRIPTIONS OF DIFFERENT CONTACT MODELS.

Hertz	This theory is suitable in the elastic state. It is unusable in the presence of adhesions and large deformations.
Lundberg	This theory calculates the elastic indentation depth caused by the compression of the two plates. In this model, the force distribution is cylindrical.
Dawson	Dawson first proposed this model to calculate the indentation depth due to the compression of a cylindrical roller between two flat plates. The force distribution in this model is cylindrical on the roller. This model assumes that the depth of the flat plate is equal to the radius of the roller.
Nikpour	This theory was first proposed to calculate the indentation depth caused by the compression of a cylindrical roller between two flat plates. The force distribution in this model is cylindrical and also considers the depth of the calcification.
Hoerich	This contact model shows the general equation of indentation depth due to the compression of a roller between two flat plates considering the depth of calcification.

$$F_m \cos \beta - F_D > \mu_s (F_m \sin \beta + W) + \tau_s A_s \rightarrow$$

$$F_m > \frac{\tau_s A_s + \mu_s W + F_D}{\cos \beta - \mu_s \sin \beta} \quad (17)$$

$$R_c (F_m \cos \beta - F_D) > \mu_{rs} (F_m \sin \beta + W) + \tau_{rs} A_s \rightarrow$$

$$F_m > \frac{\tau_{rs} A_s + \mu_{rs} W + R_c F_D}{R_c \cos \beta - \mu_{rs} \sin \beta} \quad (18)$$

III. EXPERIMENTAL SETUP FOR THE PROOF-OF-CONCEPT

A. Materials:

To synthesise magnetic nanoparticles (Fe_3O_4), ammonia (NH_3), iron (II) chloride ($FeCl_2$) ($FeCl_3 \cdot 6H_2O$) (III) with 99% purity, and iron (III) chloride ($FeCl_3$) with 99% purity from Merck were prepared. Deionized water, glycerine, and normal saline serum were purchased from the Iranian Parenteral and Pharmaceutical Company (Tehran, Iran).

- Synthesis of magnetic nanoparticles

In this study, iron oxide nanoparticles were prepared with a co-precipitation method. After the distilled water was

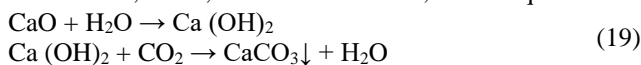
deoxygenated using an ultrasonic device, and nitrogen was passed through the water, 16.25 g of FeCl₃·6H₂O and 6.35 g of FeCl₂·4H₂O were dissolved into 200 mL of deoxygenated distilled water and stirred for 60 minutes. Next, 12 ml of the salt solution was added one drop at a time to 120 ml ammonia solution under nitrogen, and the solution was stirred for half an hour at 1000 rpm. The black precipitate was collected with a neodymium magnet, washed three times with distilled water, washed once with acetone, and dried under a vacuum. Finally, the black powder of magnetic nanoparticles was dried in an oven at 50^o C.

- Cytotoxicity evaluation

We evaluated the cytotoxicity of the magnetite nanoparticles using human macrophage cells with a primary density of 2×10⁵ cells /mm. The cells were immersed in DMEM and 10% FBS for 4, 8, 24 and 48 hours (DMEM (Dulbecco's Modified Eagle Medium) is a widely used basal medium for supporting the growth of many different mammalian cells. Foetal bovine serum (FBS) derives from the blood drawn from a bovine foetus via a closed collection system at the slaughterhouse). The percentage of viable cells was determined with a Bio-Tek EL-311 microplate reader reading at 570 nm. Various cellular concentrations of magnetite nanoparticles (5, 10, 25, 50, 100 µg/mL) were used to evaluate cellular toxicity.

- Calcification creation

The calcification layer is produced by the reaction between calcium oxide, water, and carbon dioxide, as the Eq.19:



A 1.5 mm thick calcification layer was created inside the shunt polymer tube. The mechanical property testing of the calcification appears in Table II.

TABLE II
MECHANICAL PROPERTIES OF CALCIFICATION [26]

Density	2.711 g/cm ³
Young's Modulus	69.9 GPa
Hardness (Knoop)	3 Mohs
Shear Modulus	35 GPa
Bulk Modulus	98 GPa

B. Equipment:

- Oscillating magnetic field generator prototype

The schematic of the device prototype for carrying the magnetic field appears in Fig.4(a). Given that the shunt is inside the body (from the brain to the stomach, for example), there are two approaches for removing the calcification deposit with the magnetic field, a rotational magnetic field (Ro-MF) or a reciprocating magnetic field (Re-MF). The Ro-MF method is recommended for venous thrombosis in the leg [27], in which

the magnet moves around the leg (an asymmetric organ), removing the blood clots or deposits. Considering the shape of the leg, the movement of the magnetic field applies an equal force to the surface of the sediment inside the vessel in all directions.

The second method (Re-MF) is suitable in asymmetrical scenarios. In asymmetrical conditions, the magnetic force is needed only on one side of the region of interest. As the intensity of the magnetic field decreases sharply with increasing distance, the Re-MF, in which the distance from the magnet to the deposition remains relatively constant (e. g., the prototype made in this research), can be considered a more suitable approach for asymmetrical conditions.

In this method, the magnetic field can be moved around the body. The large distance between the magnet and the surface of the shunt will induce a sharp decrease in the magnetic field. The second method involves oscillating the magnetic field close to the surface of the shunt. For this study, we developed a prototype device for the oscillating approach.

The device was made using 3D printing (biocompatible polylactic acid (PLA)). A stepper motor controlled by a programmable logic controller (PLC) moved the magnets precisely. A permanent magnet that moves with various frequencies and oscillation lengths was placed on the device. Furthermore, these experiments used a commercial shunt from the company G. Surgiwear Ltd. The shunt had a diameter of 5 mm. Fig.4(a) shows the thickness of the calcification layer and the position of the permanent magnet.

C. Experimental setting:

In these experiments, the input parameters include the magnetic field strength (0.1, 0.15, 0.22, and 0.3 T), the number of oscillation cycles (3500, 7000, 10000, and 11000), and the oscillation speed (1, 3, 6, 9, and 12 cm/s). The output of the experiments was the percentage of calcification layers that were abraded. For this purpose, the weight of the calcification layer was measured before and after the abrading process. Eq.20 was used to obtain the percentage of the calcification abrasion rate. ImageJ software obtained the nanoparticle size (Table III).

$$\text{Calcification abrading rate (\%)} = \frac{\text{initial weight} - \text{final weight}}{\text{initial weight}} \times 100 \quad (20)$$

TABLE III
EXPERIMENTAL SETTING

Parameter	value
Size of the magnetic nanoparticles	50 nm
Magnetic nanoparticle dosage	50 mg
The geometry of the channel	circular channel with 5 mm diameter
Fluid	Normal saline

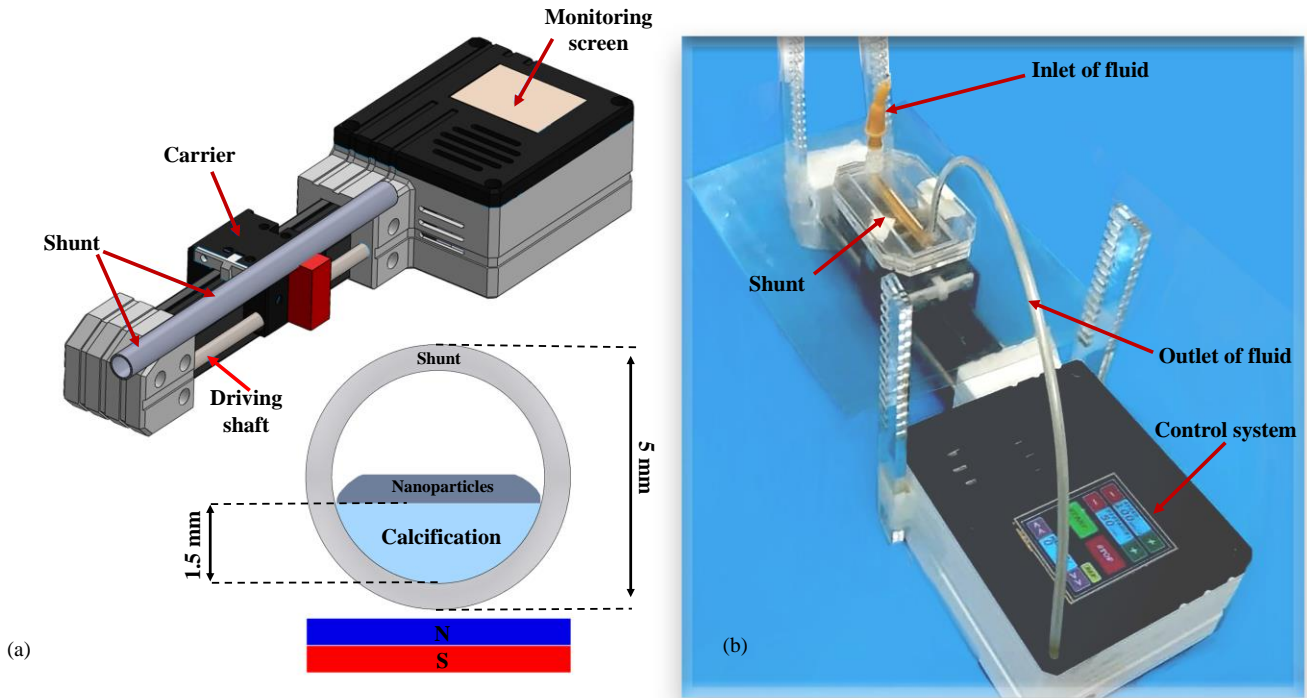


Fig.4. (a) The schematic of the prototype device for carrying the magnetic field. (b) The prototype device for the experiments.

Transmission electron microscopy (TEM) (JEM-2000 EX II; JEOL, Tokyo, Japan) estimated the size of the magnetic nanoparticles (Fig.5 (a)). Fig.5(b) shows that the nanoparticles had an average diameter of 45 nm with a semi-spherical shape.

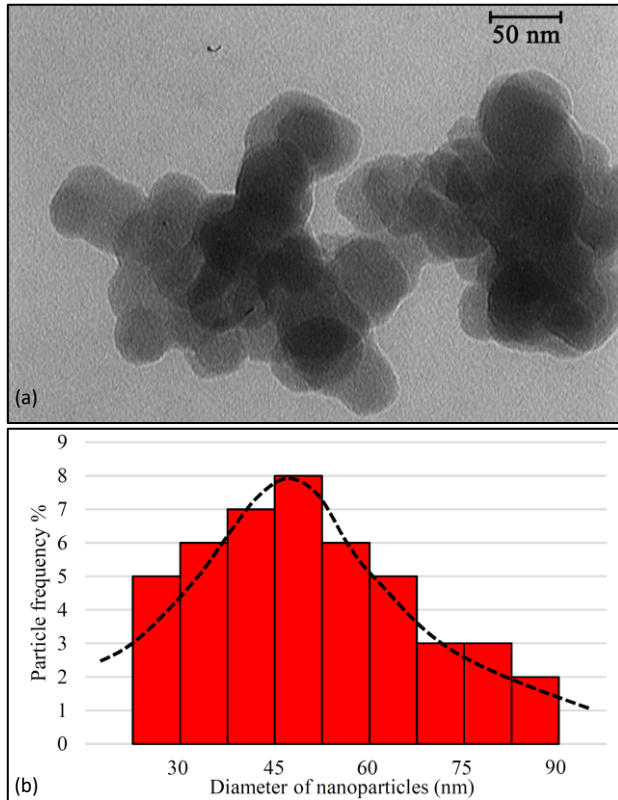


Fig.5. Magnetic nanoparticle size. (a) TEM image of magnetic nanoparticles. (b) Histogram of magnetic nanoparticle size.

The magnetization properties were measured with a vibrating magnetometer (VSM 7400 Lake Shore). The saturation

magnetization (M_s) and retentivity (M_r) values of the synthesized magnetic nanoparticles were $49.62 \text{ (Am}^2/\text{kg)}$ and $2.456 \text{ (Am}^2/\text{kg)}$, respectively (Fig.6).

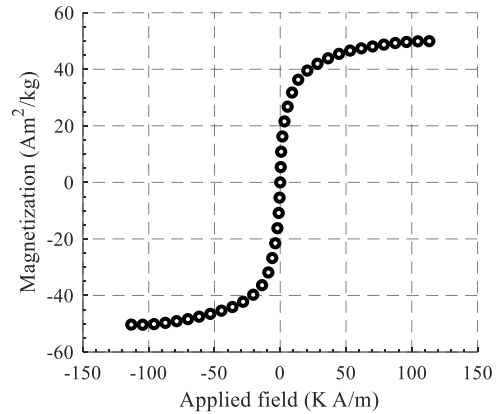


Fig.6. The vibrating-sample magnetometer (VSM) analyses of magnetic nanoparticles.

IV. SIMULATION AND RESULTS

A. Simulation of contact mechanics

This section presents the simulation results of contact theories. The purpose of these simulations was to obtain the deformation range caused by the magnetic force applied to the nanoparticles. In Fig.7, the indentation depth diagram is plotted with respect to force. This diagram considers various magnetic fields. According to the equations presented (Eq.7 to Eq.12), as the magnetic field increases, the amount of magnetic force increases. Based on these equations, the indentation depth is directly linked to the magnetic force.

Thus, according to the Hoyerich theory, the maximum amount of deformation in $B=0.3 \text{ T}$ is 4.4 nm , in $B=0.22 \text{ T}$ is 2.4

nm, in $B = 0.15 \text{ T}$ is 1.9 nm , and in $B = 0.1 \text{ T}$ is 1.2 nm . Based on Eq.12, the Hoeprich theory could calculate a large deformation.

In all the simulations, the Hertz and Lundberg theories had the lowest indentation depths. This result is because these theories only apply to small deformations. Given the similarities between the Nikpur and Dowson theories, the amount of deformation created with these two theories was very similar.

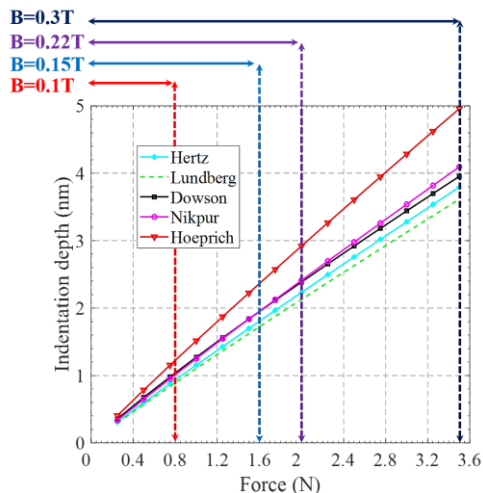
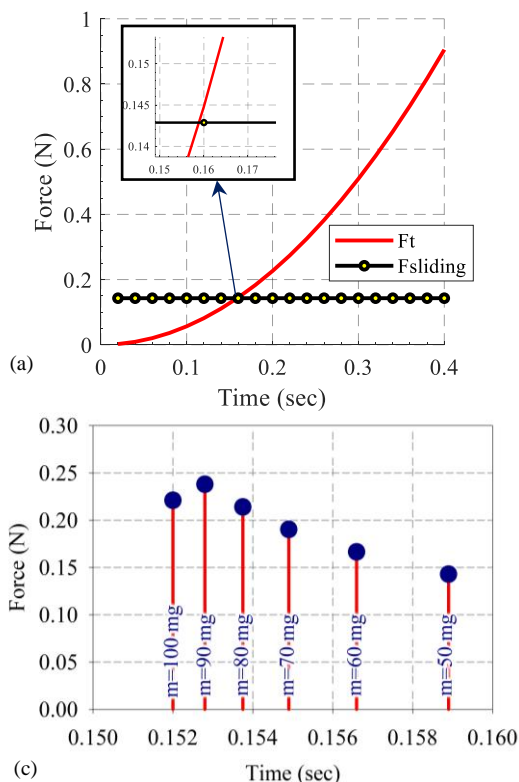


Fig.7. The relation between different indentation depth models and magnetic force (under various magnetic fields).

B. Simulation of the microswarm movement

For dominant mode calculation, we first obtained the initial conditions, including geometry, contact mechanics, and magnetic force. The set of forces acting on the nanoparticles



was then calculated using Eq.17 and Eq.18. If this calculated force was greater than the friction, then oscillation began. The dominant motion mode could be predicted based on the magnitude of the force and the type of friction.

The microswarm motion modes appear in Fig.8. For the condition presented in Table IV (Due to the complexity of calculating the properties of microswarm, this section uses the properties of a nanoparticle), sliding occurred first. According to Fig.8(a), after 0.16 seconds and with 0.143 N force, the microswarm started sliding. The rolling mode occurred with 23.09 KN force in 63.77 seconds (Fig.8(b)). The dominant mode of motion determines the amount of force which is required to move the microswarm. Finally, the required magnetic field and its range can be predicted using the force magnitude. Figs.8(c) and 8(d) display the force and time with respect to the mass. As the particle mass increases, the critical time will decrease, and critical force will increase. This result was expected since the mass increases particle dimension and contact area. Therefore, the total force will increase, which promotes faster particle movement.

TABLE IV
CONDITIONS IMPLEMENTED FOR A SINGLE NANOPARTICLE

Mass (mg)	Modulus of elasticity (G pa)	Poisson ratio	μ_s	μ_{rs}	$\rho(\frac{\text{kg}}{\text{m}^3})$
50	170	0.37	0.1	0.8	1000

Finally, from the simulation results (Fig. 8), the upper limit for the force required to start particle movement was 0.15 N. Therefore, the magnetic field with 0.3 T intensity is safe for the proposed approach.

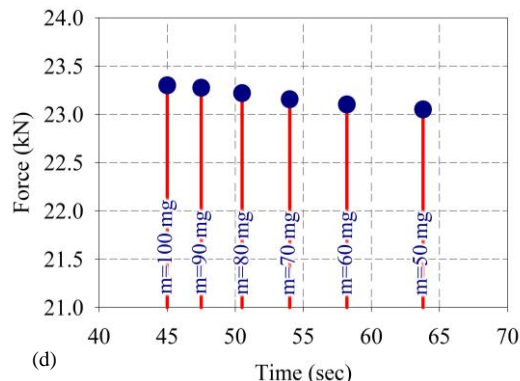
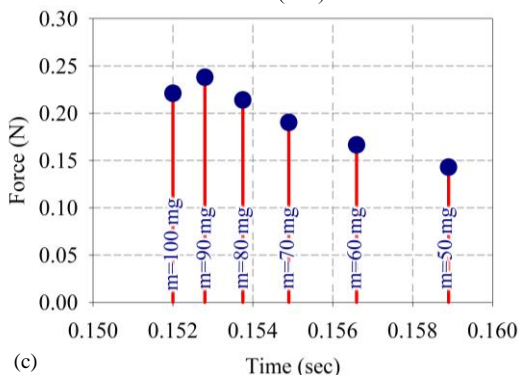
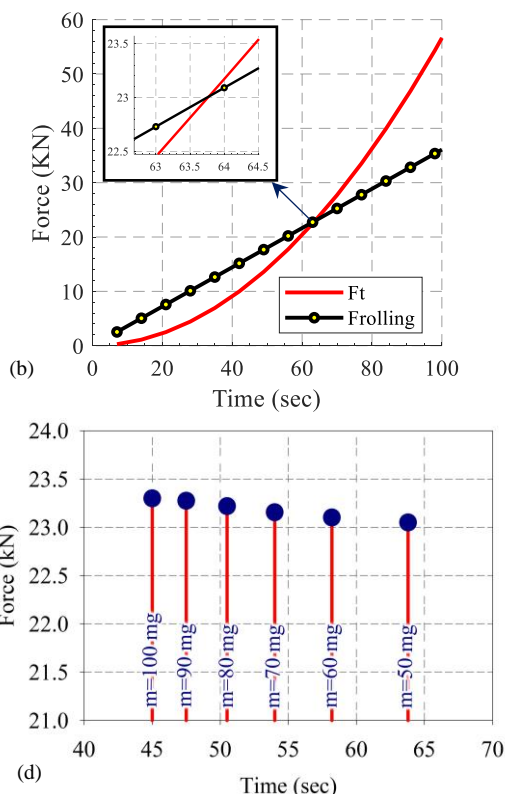


Fig.8. The type of motion modes (sliding and rolling mode). (a) Sliding mode; (b) rolling mode; (c) critical time and force for different mass (sliding); (d) critical time and force for different mass (rolling).

C. Experimental results

The proof-of-concept experiments assessed the proposed technique. All experiments were performed three times. The results confirmed that the proposed strategy could remove the calcification layers in the shunt. Fig.9(a) shows that the calcification layer in the interior of the shunt was removed in the direction of the magnet movement.

The effect of the magnetic field strength and the velocity of the magnetic oscillation on the calcification removal were also examined. Increasing the intensity of the magnetic field leads to an increase in the removal (Fig.9(b)). The indentation depth in the calcification layers caused by the magnetic nanoparticles increases when the magnetic field increases. A 0.1 T magnetic field strength required 60 minutes to remove 100% calcification. Increasing the magnetic field strength to 0.3 T decreased the time to 20 minutes. Furthermore, the amount of calcification wear increased with increasing magnetic field strength. Increasing the intensity of the magnetic field elevated the force exerted on the magnetic nanoparticles, which ultimately produced greater penetration of the calcification surface by the magnetic nanoparticles. Therefore, increasing the normal force will increase the indentation rate of the nanoparticle at the target surface, as shown in Fig.9(b).

The magnetic force has two components with respect to the deposition removal direction, the normal and tangential components. The normal component leads to penetration of the surface by the magnetic force. The tangential component is due

to friction (an indirect effect of the magnetic force).

The tangential component leads to substance removal from the surface. The forces appear in Fig.3. The ideal case ($\beta=0$) is used to explain the mechanism. Increasing the magnetic field intensity (normal component) elevates the surface penetration by the nanoparticles (abrasive tool), which results in higher material removal rate.

The effect of the oscillation velocity on the abrading rate of the calcification appears in Fig.9(c). The experimental results show that, as expected, there is a direct relation between the speed of the magnetic field and the rate of calcification abrading. However, as the speed of the movement of the magnetic field increases, the amount of the calcification removal will decrease sharply, which is linked to the step-out frequency. This result can be attributed to the fact that as the magnetic field travels faster, the magnetic nanoparticles cannot follow it (velocity=12 cm/s). Under high-velocity magnetic field oscillation, abrasive microswarms cannot remove calcification. Therefore, the process should set an upper speed limit. All samples were measured for 10 minutes, but the velocity=9 cm/s reached 100% wear in 7 minutes.

On the other hand, the field movement velocity affects the material removal rate. The faster magnetic nanoparticles move, the more calcification will be removed. Although an increase in the removal is observed with the rise in the velocity, once it passes the maximum threshold limit (depending on the material properties of the abrading particles), the particles cannot follow the field, and the particle removal will decrease significantly (shown in Fig. 9(c)).

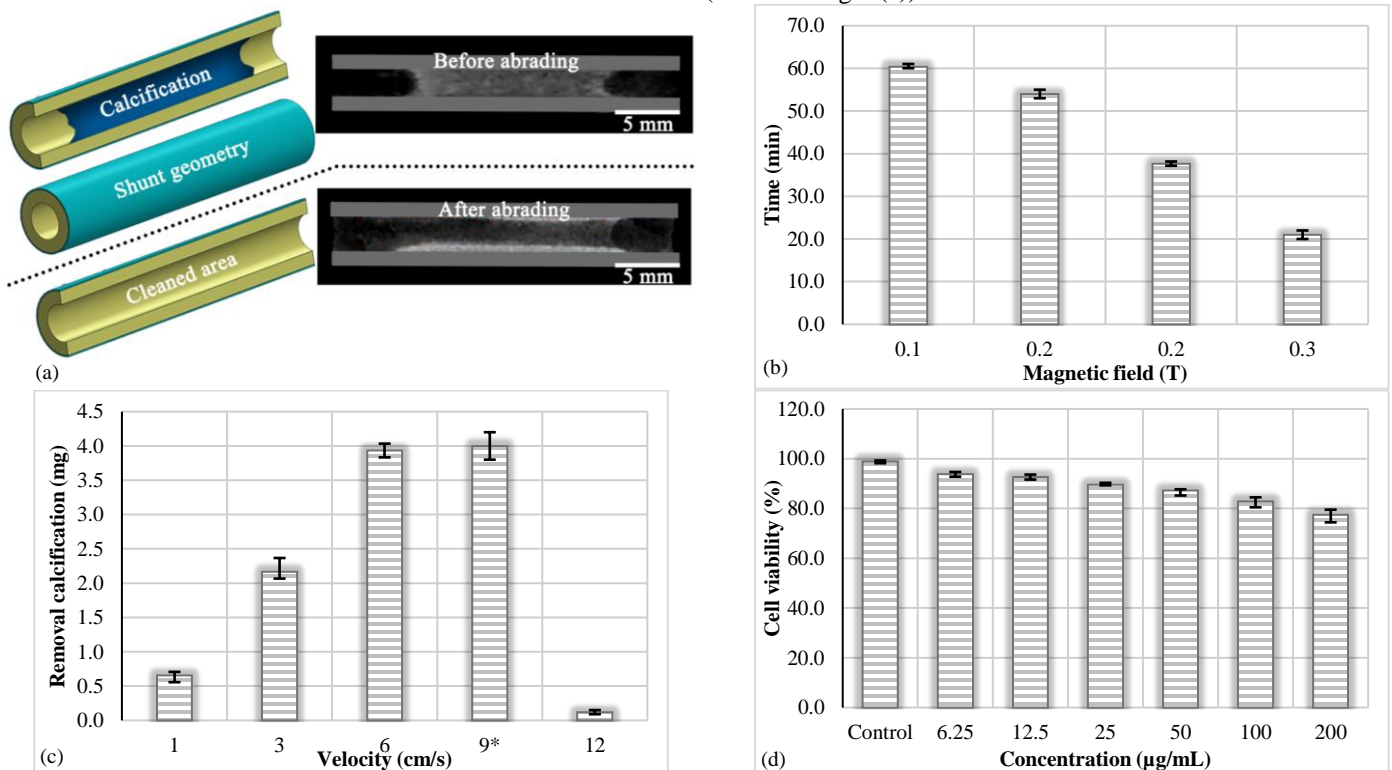


Fig 9. (a) Radiographic and schematic image of the calcification shunt. (b) The effect of the magnetic field strength on the total layer removal time. Individual standard deviations were used to calculate the intervals (95% CI for the mean). (c) The calcification removal layer for different oscillating field velocities; the magnetic field was 0.3 T, and the processing time was 10 min (* note, for 9 cm/s, the total removal was achieved at 7 minutes). Individual standard deviations were used to calculate the intervals (95% CI for the mean). (d) The cell viability of macrophage cells following exposure to magnetic nanoparticles was assayed with MTT after 24 hrs (* $p < 0.001$ analysed with a one-way ANOVA versus control groups).

The magnetic abrasive finishing (MAF) process (a non-traditional manufacturing process) follows a similar removal mechanism [28]. The link between abrading particles' rotational speed and material removal is also reported in [29].

The biocompatibility of the nanoparticles was also investigated at different concentrations of Fe_3O_4 for 24 hours, as shown in Fig. 9(d). This experiment showed that concentrations lower than $100 \mu\text{g/mL}$ had minor effects on cytotoxicity. After intravenous injection, the magnetic nanoparticles may interact with extracellular matrix components, the plasma cell membranes of macrophages, and endothelial cells [30]. Therefore, it is vital to study the biocompatibility of magnetic nanoparticles. Various concentrations of magnetic nanoparticles at different times showed cellular biocompatibility. As illustrated in Fig.9(d), the Fe_3O_4 nanoparticles exhibited almost no toxicity in the range of $6.25\text{--}50 \mu\text{g/mL}$ for human macrophages, while observable toxicity was detected at $200 \mu\text{g/mL}$. Therefore, increasing the concentration of magnetic nanoparticles leads to escalating cytotoxicity. In addition, cytotoxicity will increase with increasing cell incubation times. Therefore, Fe_3O_4 is not toxic to human macrophage cells at low concentrations.

V. VALIDATION

This section describes the validation of the outputs following the simulation and experiments, as shown in Fig 10. It displays the force diagram in terms of an indentation depth for the 0.3 T magnetic field (Fig.10(a)). We used an indirect method to measure the indentation depth experimentally. First, the mass of the removed calcification layer is measured for a specific number of oscillations. Then the mass is calculated for each oscillating motion. Next, considering the number of nanoparticles in contact with the surface (from geometry), the amount of mass removed per nanoparticle is estimated [27,31,32].

Fig.10 (b) shows the error rate based on the experimental results. The Lundberg and Hertz theories showed the lowest indentation depth. These theories are appropriate when the indentation depth is shallow. Since these two theories only apply to small deformation states, their simple equations cannot predict large deformations. The Dowson and Nikpur theories produced relatively similar results.

The Hoeprich theory is more suitable for calculating a large degree of deformation. As the force increases, the adaptation of this theory to the experimental results increases. In general, the Hoeprich model has a sizeable deformation nature. When the applied force increases, this model can predict the amount of deformation better than other models. The Hoeprich model can therefore estimate the force needed for calcification removal (12.1% deviation). For the Dowson, Nikpur, Lundberg and Hoeprich theories, this value was 12.6%, 13.2%, 19.7% and 21.4%, respectively.

VI. CONCLUSION

This research study provides a new, non-invasive intervention technique to eliminate shunt calcifications wirelessly by using magnetic nanoparticles. The non-invasive nature of this method is a considerable advantage, potentially eliminating the risk of surgery-related infection, decreasing recovery time, and elevating patient satisfaction. One of the challenges is limiting the intensity of the magnetic field applied to the patient. In the proof-of-concept experiments, the distance

between the shunt and the magnetic field was 2 mm to enable the testing of a range of magnetic fields. However, in realistic scenarios, the shunt is placed inside the body where the distance is greater than 2 cm. To mitigate this drawback, researchers should use stronger permanent magnets. The next step of this research is to perform *in vivo* studies.

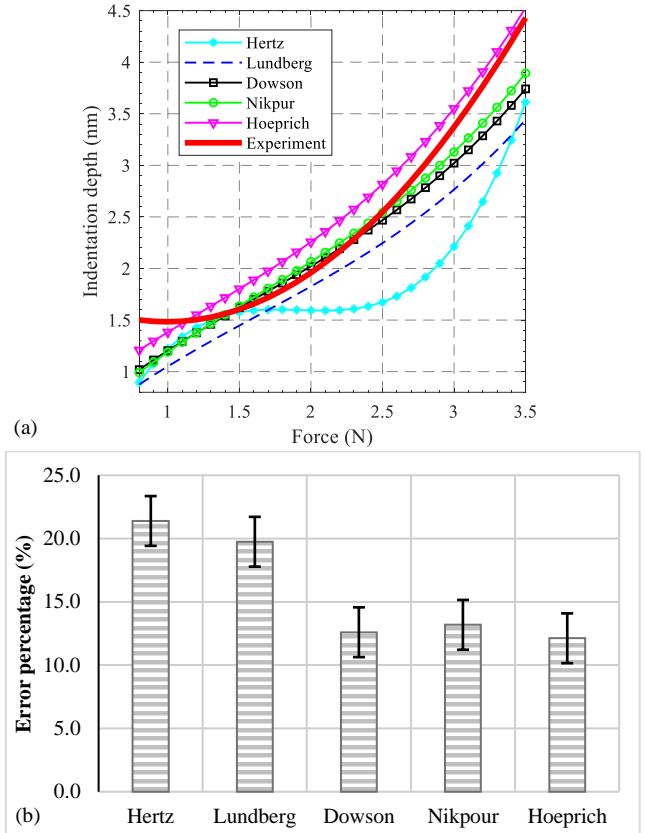


Fig.10. (a) Comparison between the experimental results and the simulation results (magnetic field 0.3 T). (b) Error percentage based on the experimental results.

The experimental results showed that as the magnetic intensity increased from 0.1 T to 0.3 T, the time required to remove the calcification layer reduced by 33%. Increasing the frequency of the magnetic field oscillation from 1 cm/s to 9 cm/s caused a notable increase in the removal of the calcification layer initially. However, after reaching the step-out frequency (12 cm/s speed), the rate of calcification removal decreased since the nanoparticles could not follow the field. To simulate the movement of the magnetic nanoparticles, two modes of motion—sliding and rolling—were evaluated. The results showed that the sliding mode was the most suitable for this process. The experimental data were consistent with the theoretical predictive model. Five contact models, including Hertz, Lundberg, Dowson, Nikpur and Hoeprich, were investigated to calculate the indentation depth. The results showed that the Hoeprich theory was the ideal option, with a 12.1% error.

AUTHOR CONTRIBUTIONS

A.K.H. conceived and designed the study. H.K. and A.K.H. developed the simulation models. A.M. self-funded and performed the experiments. A. M and H. K jointly wrote the manuscript. All authors have read and agreed to the published version of the manuscript.

REFERENCES

1. R. Bhardwaj, H. Vaziri, A. Gautam, E. Ballesteros, D. Karimeddini, and G. Y. Wu, "Chylous Ascites: A Review of Pathogenesis, Diagnosis and Treatment," *J. Clin. Transl. Hepatol.*, vol. 6, no. 1, pp. 1–9, 2018.
2. Y. Chen, "Parameter Optimization and in Vitro Evaluation of Implantable Medical Devices. University of Pittsburgh, 2018.
3. K.-A. S. Mitchell et al., "The impact of hydrocephalus shunt devices on quality of life," *J. Craniofac. Surg.*, vol. 32, no. 5, pp. 1746–1750, 2021.
4. P. Prakash, M. Dhandapani, S. Ghai, N. V. Singh, and S. Dhandapani, "Quality of life among children who had undergone ventriculoperitoneal shunt surgery," *J. Pediatr. Neurosci.*, vol. 13, no. 2, pp. 189–194, 2018.
5. J. Cameron-Lawson, "Neonatal intensive care nurses using evidence-based practice innovations to control escalating healthcare cost," Barry University, 2021.
6. M. Swoboda, M. G. Hochman, J. S. Fritz, M. E. Mattiucci, and F. J. Fritz, "A new method for CSF shunt patency assessment," *Neurodx.com*. [Online]. Available: <https://neurodx.com/wp-content/uploads/2017/10/Swoboda-2013-A-new-method-for-CSF-shunt-patency-assessment.pdf>. [Accessed: 20-Nov-2021].
7. M. I. Chavez et al., "Distal splenorenal and mesocaval shunting at the time of pancreatectomy," *Surgery*, vol. 165, no. 2, pp. 298–306, 2019.
8. S. A. Mirjalili, L. Hinton, and S. Richards, "Gastrointestinal Physiology," in *Physiology for General Surgical Sciences Examination (GSSE)*: Springer, pp. 37–54, 2019.
9. C. Lin, L. Liu, Y. Liu, and J. Leng, "Recent developments in next-generation occlusion devices," *Acta Biomater.*, vol. 128, pp. 100–119, 2021.
10. H. J. Carpenter, A. Gholipour, M. H. Ghayesh, A. C. Zander, and P. J. Psaltis, "A review on the biomechanics of coronary arteries," *Int. J. Eng. Sci.*, vol. 147, no. 103201, p. 103201, 2020.
11. E. Aminov, "University of California, San Diego," University of California, 2017.
12. S. R. Krishnan et al., "Epidermal electronics for noninvasive, wireless, quantitative assessment of ventricular shunt function in patients with hydrocephalus," *Sci. Transl. Med.*, vol. 10, no. 465, p. eaat8437, 2018.
13. T. M. Downing, S. N. Khan, R. C. Zvavanjanja, Z. Bhatti, A. K. Pillai, and S. T. Kee, "Portal venous interventions: How to recognize, avoid, or get out of trouble in transjugular intrahepatic portosystemic shunt (TIPS), balloon occlusion sclerosis (ie, BRTO), and portal vein embolization (PVE)," *Tech. Vasc. Interv. Radiol.*, vol. 21, no. 4, pp. 267–287, 2018.
14. H. J. Ginsberg, J. M. Drake, and R. S. C. Cobbold, "Unblocking cerebrospinal fluid shunts using low frequency ultrasonic cavitation," in 2001 IEEE Ultrasonics Symposium. Proceedings. An International Symposium (Cat. No.01CH37263), 2002, vol. 2, pp. 1381–1384 vol.2.
15. L. Magrassi et al., "Minimally invasive procedure for removal of infected ventriculoatrial shunts," *Acta Neurochir. (Wien)*, vol. 163, no. 2, pp. 455–462, 2021.
16. M. Preul et al., "Laser application in neurosurgery," *Surg. Neurol. Int.*, vol. 8, no. 1, p. 274, 2017.
17. L. Manamanchaiyaporn, X. Tang, Y. Zheng, and X. Yan, "Molecular transport of a magnetic nanoparticle swarm towards thrombolytic therapy," *IEEE Robot. Autom. Lett.*, vol. 6, no. 3, pp. 5605–5612, 2021.
18. K. Abolfathi, M. R. H. Yazdi, and A. K. Hoshjar, "Studies of different swarm modes for the MNPs under the rotating magnetic field," *IEEE Trans. Nanotechnol.*, vol. 19, pp. 849–855, 2020.
19. J. Jiang, L. Yang, and L. Zhang, "Closed-loop control of a Helmholtz coil system for accurate actuation of magnetic microrobot swarms," *IEEE Robot. Autom. Lett.*, vol. 6, no. 2, pp. 827–834, 2021.
20. Q. Wang, L. Yang, J. Yu, P. W. Y. Chiu, Y.-P. Zheng, and L. Zhang, "Real-time magnetic navigation of a rotating colloidal microswarm under ultrasound guidance," *IEEE Trans. Biomed. Eng.*, vol. 67, no. 12, pp. 3403–3412, 2020.
21. H. Hertz, "Über die Berührung fester elastischer Körper," *J. Reine Angew. Math.* vol. 92, pp. 156–171, 1881.
22. G. Lundberg, "Elastische Berührung zweier Halbraume," *Forschung AUF dem Gebiete der Ingenieurwesens*. Vol. 10, No. 5, pp. 20, 1939.
23. D. Dowson and G. R. Higginson, "Theory of roller bearing lubrication and deformation," in *Proceedings of Lubrication and Wear Convention (Institute of Mechanical Engineering, London)*, Paper 19, pp. 216–227, 1963.
24. K. Nikpur and R. Gohar, "Deflection of a roller compressed between plates," *Tribol. Int.* vol.8, pp. 2–8, 1975.
25. M. R. Hoeprich and H. Zantopulos, "Line contact deformation: A cylinder between two flat plates," *ASME J. Lubr. Technol.* vol. 103, pp. 21–25, 1981.
26. M. Portigliatti Barbos, P. Bianco, and A. Ascenzi, "Distribution of osteonic and interstitial components in the human femoral shaft with reference to structure, calcification and mechanical properties," *Acta Anat. (Basel)*, vol. 115, no. 2, pp. 178–186, 1983.
27. A. Moghanizadeh, F. Ashrafizadeh, J. Varshosaz, M. Kharaziha, and A. Ferreira, "Noninvasive thrombectomy of graft by nano-magnetic ablating particles," *Sci. Rep.*, vol. 11, no. 1, p. 7004, 2021.
28. T. Al-Dulaimi and M. B. Khamesee, "A stationary apparatus of magnetic abrasive finishing using a rotating magnetic field," *Microsyst. Technol.*, vol. 23, no. 11, pp. 5185–5191, 2017.
29. C. Prakash et al., "Experimental investigation into nano-finishing of β -TNTZ alloy using magnetorheological fluid magnetic abrasive finishing process for orthopedic applications," *J. Mater. Res. Technol.*, vol. 11, pp. 600–617, 2021.
30. A. B. Engin et al., "Mechanistic understanding of nanoparticles' interactions with extracellular matrix: the cell and immune system," *Part. Fibre Toxicol.*, vol. 14, no. 1, 2017.
31. V. K. Jain, S. C. Jayswal, and P. M. Dixit, "Modeling and simulation of surface roughness in magnetic abrasive finishing using non-uniform surface profiles," *Mater. Manuf. Process.*, vol. 22, no. 2, pp. 256–270, 2007.
32. P. Kala, V. Sharma, and P. M. Pandey, "Surface roughness modelling for Double Disk Magnetic Abrasive Finishing process," *J. Manuf. Process.*, vol. 25, pp. 37–48, 2017.